31st Congress of the International Council of the Aeronautical Sciences

Belo Horizonte, Brazil; September 09-14, 2018

PROPELLER INFLUENCE ON THE STABILITY OF HALE AIRCRAFT

Patricia C. Teixeira , Carlos E. S. Cesnik
University of Michigan

Keywords: *propeller effects, HALE, aeroelastic stability*

Abstract

This work investigates the propeller influence on the stability of High Altitude Long Endurance aircraft by the inclusion of propeller slipstream and gyroscopic effects usually neglected in the aeroelastic simulation of HALE aircraft. For that goal, a previously developed framework, which couples a geometrically nonlinear structural solver with an Unsteady Vortex Lattice method (uVLM) for lifting surfaces and a Viscous Vortex Particle (VVP) method for propeller slipstream, was employed to generate time-data series. Also, a method to extract frequencies, damping, and modes of the aircraft from snapshots data based on a combination of Proper Orthogonal Decomposition and system identification is proposed and successfully tested for a purely structural case, for which reference data is available. The method is then applied to investigate the stability of aeroelastic cases. Results suggest the propeller influence on the stability boundary of the HALE model studied.

1 Introduction

In recent decades a new concept of unmanned air vehicle (UAV) has received increased attention due to its low energy consumption and promising applications: High-Altitude Long Endurance (HALE) aircraft. In order to achieve their higher aerodynamic performance, HALE aircraft are typically high-aspect-ratio configurations, resulting in a very flexible structure, which imposes additional challenges to the aircraft stability and control. Also, due to the typical low cruise speed, a propeller-motor combination is often the choice of propulsion. As pointed out in previous works, such as Phillips [1], Ribner [2], and Bouquet [3], the different propeller effects can potentially impose significant effects on the stability of an aircraft. However, in the aeroelastic analysis of a very flexible aircraft, the modeling of propeller effects is usually reduced to just a concentrated force and little has been explored about the influence of propeller effects on the aircraft rigid body and aeroelastic stability in the context of a very flexible structure. Previous works like Hodges *et al.* [4], Feldt and Herrmann [5] and Quanlong *et al.* [6] have demonstrated that follower thrust has an important influence on the aeroelastic stability of a very flexible wing, causing differences of about 10% in flutter prediction. Little have been explored, however, about other propeller effects, mainly propeller slipstream and gyroscopic moment, on the aeroelastic stability of very flexible HALE aircraft.

This paper has the objective of investigating the influence of propeller thrust, slipstream and, gyroscopic moment on the aeroelastic stability of a very flexible HALE aircraft.

2 Aeroelastic Framework with Propeller

The nonlinear aeroelastic framework for this study must include the couplings with the flight mechanics equations of motion. The point of departure for it is the University of Michigan's Nonlinear Aeroelastic Simulation Toolbox (UM/NAST) [7]. The various components of this

framework are described next.

2.1 Structural Model

The structural model is based on a geometrically nonlinear structural formulation using a strain-based nonlinear finite element model of Su and Cesnik [8]. In this approach, constant strain in extension, twist, and in- and out-of-plane bending is assumed inside each beam element. Nonlinear equations of motion are also solved in terms of those strain values and the related displacements are post processed.

2.2 Lifting Surface Aerodynamic Model

The original aerodynamic model in UM/NAST employed a corrected strip theory. However, in order to incorporate the aerodynamic propeller effects, a method that allows to take into account the mutual influence among lifting surfaces is necessary. For this purpose, an Unsteady Vortex Lattice code developed by Ritter *et al.* [9] was coupled to UM/NAST. As observed there, the uVLM solver is capable to model translations and rotations of the panels due to arbitrary elastic deformations, allowing simulations with large structural displacements. Also, it has a smaller computational cost compared to unsteady RANS solution. The modeling of induced and profile drag is also included. In order to estimate the profile drag, the effective angle of attack at each strip is determined based on the average effective angle of attack of each panel along the strip. The corresponding drag coefficient is determined based on a polar table (*e.g.*, XFOIL).

2.3 Incorporating Propeller Effects

2.3.1 Propeller Aerodynamics

For the propeller aerodynamic modeling, two methods were coupled: lifting line to model blade bound circulation, and Viscous Vortex Particle (VVP) to model propeller slipstream. The VVP formulation is a Lagrangian approach based on the vorticity-velocity equation of incompressible flows, *i.e.*,

$$D\vec{\omega}/dt = \vec{\omega}.\nabla\vec{u} + \nu\nabla^2\vec{\omega} \tag{1}$$

where $\vec{\omega}$ is the vorticity field, $\vec{u}$ is the associated velocity field, and ν is the kinematic viscosity. The basic idea of VVP is that the vorticity field can be discretized by n_p vortex particles and written as the sum of each individual vorticity field:

$$\vec{\omega}(\vec{x},t) = \sum_{i=1}^{n_p} \varepsilon_\sigma(\vec{x}-\vec{x}_i)\vec{\alpha}_i = \sum_{i=1}^{n_p} \varepsilon_\sigma(\vec{x}-\vec{x}_i)\vec{\omega}_i Vol_i \tag{2}$$

where $\vec{x}_i$ and $\vec{\alpha}_i$ are the position and strength associated with particle i, respectively. Also, ε is a distribution function associated to the particle vorticity field, and ε_σ is defined as $\varepsilon_\sigma = \varepsilon/\sigma^3$. In this work, a Gaussian distribution for σ is used as done by Singh and Friedmann [10] and He and Zhao [11]. σ is a smoothing parameter and for convergence it should be as minimum as possible, but greater than the minimum typical distance between two particles (core overlapping condition)[12, 11] which defines the flow-field resolution. At each time step new vortex particles are generated from each blade segment satisfying vorticity conservation: shed particles, related to the variation of circulation on each blade segment with time, and trailing particles, related to the spatial variation of circulation along blades. Combining Eqs. 1 and 2 the following governing equations to update particle positions and strength can be obtained:

$$D\vec{\alpha}/Dt = \vec{\alpha}.\nabla\vec{u} + \nu\nabla^2\vec{\alpha} \tag{3}$$

$$\vec{u} = -\sum_{i=1}^{n_p} 1/\sigma_i^3 K(\rho)(\vec{x}-\vec{x}_i) \times \alpha_i \tag{4}$$

where $\rho = |\vec{x}-\vec{x}_i|/\sigma_i$ is a nondimensional distance parameters and $K(\rho)$ is the Biot-Sarvat kernel. A point of concern in VVP is that for N particles it has a characteristic speed of $O(N^2)$. Then, as the number of particles increases with time, the computational cost increases significantly and some acceleration procedure may be necessary. In this work a cut-off distance is applied when particles are sufficiently far away from the region

of interest. More details about VVP formulation can be found in Winckelmans and Leonard [12] and in He and Zhao [11].

2.3.2 *Propeller Inertial Effects*

The derivation of propeller inertia formulation is described in details in previous work by the authors [13] and for conciseness it will not be repeated here. Considering a structural model for the propeller in which each blade is represented by a rigid, massless rod with a distribution of concentrated masses and assuming that the propeller configuration is such that: i) all blades have the same geometry and mass distribution, and ii) same angle between adjacent blades, one can find that the inertial loads acting on the propeller are equivalent to the inertial loads acting on a punctual mass m_p located at the propeller hub plus a moment contribution which accounts for gyroscopic effects of the rotating blades, given by:

$$\vec{M}_{rot} = \sum_{k=1}^{N_{seg}} \sum_{i=1}^{N_{blades}} -m_k[\,\vec{p}_{i,k} \times (\ddot{\vec{p}}_{i,k} + 2\,{}^I\vec{\omega}^B \times \dot{\vec{p}}_{i,k} + {}^I\dot{\vec{\omega}}^B \times \vec{p}_{i,k} + {}^I\vec{\omega}^B \times {}^I\vec{\omega}^B \times \vec{p}_{i,k})] \tag{5}$$

with:

$$\dot{\vec{p}}_{i,k} = ({}^B\vec{\omega}^P + {}^P\vec{\omega}^b) \times \vec{p}_{i,k} \tag{6}$$

$$\ddot{\vec{p}}_{i,k} = {}^B\dot{\vec{\omega}}^P\,{}^b\vec{p}_{i,k} + ({}^B\vec{\omega}^P + {}^P\vec{\omega}^b) \times ({}^B\vec{\omega}^P + {}^P\vec{\omega}^b) \times \vec{p}_{i,k} \tag{7}$$

where N_{blades} and N_{seg} are the number of blades and blades segments, respectively, m_k is the mass of a concentrated mass located at blade segment k, $\vec{p}_{i,k}$ is the position of the concentrated mass with relation to a frame attached to the propeller hub, ${}^I\vec{\omega}^B$ is the angular velocity of the body with relation to an inertial frame, ${}^B\vec{\omega}^P$ is the angular velocity of propeller frame with relation to body frame, and ${}^P\vec{\omega}^b$ is the angular velocity of blade frame with relation to propeller frame (given by propeller rotation per unit time). Also, all derivatives are defined in the body frame.

3 Extracting Dynamic Information with POD + System Identification

Due to the challenge of determining a linearized analytical solution with propellers in the frequency domain an alternative approach is used to analyze stability. For this, using snapshots obtained from time simulation, an input-output based system identification approach is employed to build a mathematical model of the system in state form, i. e.,

$$\dot{x}(t) = A\,x(t) + B\,u(t) + K\,e(t) \tag{8}$$

$$y(t) = C\,x(t) + K\,e(t) \tag{9}$$

where A, B, C, and D are the estimated matrices of state space, K a matrix which accounts by disturbances, $u(t)$ is the input, $y(t)$ is the output and $x(t)$ is a vector with n_x states associated with this mathematical representation. The identification was performed using the tool `n4sid` available on Matlab and more details about the method can be found in Van Overschee and De Moor [14]. For the present case, the identification is done by providing a matrix containing the values of applied loads at each time step (inputs) and a matrix of snapshots containing the displacements (in x,y and z directions) of each structural node with relation to an initial equilibrium condition (outputs). The system identification has been found to have a better performance for a small number of degrees of freedom (d.o.f.). However, this is not the case of a flexible aircraft with the framework employed here (the model considered later, for example, has more than 500 d.o.f.) and the direct application of system identification becomes difficult. In order to overcome this limitation, instead of providing directly the output matrix containing the snapshots of displacements, the snapshots containing the coefficients of a much smaller number of POD modes is provided. For this, Singular Value Decomposition is first applied to the output matrix M:

$$M_{m\times n} = U_{m\times m}\,\Sigma_{m\times n}\,V^T_{n\times n} \tag{10}$$

where m is the number of d.o.f., n is the number of snapshots, U and V are orthogonal ma-

trices containing left-singular vectors and right-singular vectors of M, with the columns of U corresponding to the POD modes, and Σ is a diagonal matrix of non-negative real number ordered in descending order. Also, the product $\Sigma_{m\times n}\ V^T_{n\times n}$ is associated with the coefficients of the POD modes which reconstitute the matrix M. The value of Σ diagonal entries is associated with the importance of the POD mode to represent the data given by matrix M. Then, based on the ratio of the sum of the diagonal entries until a given column i over the trace of matrix M, the number of modes can be determined under some tolerance criteria. Usually, the first few POD modes are responsible for more than 99% of the trace. Reducing the number of POD modes to p, one obtains the new output matrix containing snapshots of the coefficients of the p POD modes which approximate the matrix M where $p << m$. For this, a reduced singular value decomposition representation of M can be found by using just the p POD modes selected as:

$$M_{m\times n} = U_{r,m\times p}\ \Sigma_{r,p\times p}\ V^T_{r,p\times n} \tag{11}$$

The new reduced output matrix N provided to the system identification is then given by:

$$N_{p\times n} = \Sigma_{p\times p}\ V^T_{p\times n} \tag{12}$$

Based on this reduced output matrix representation and the matrix containing snapshots with the input values, the matrices in equations 8 and 9 are determined. The dynamic information in terms of frequency, damping, and modes can be obtained by extracting and post-processing the eigenvalues and eigenvectors of A.

Considering E as the matrix with the eigenvectors of A (remembering they are related to coefficients of the chosen POD's) and by equation 9, the modes in terms of displacements at structural nodes can be recovered by:

$$N_{p\times n} = U_{r,m\times p} C_{p\times k} E_{k\times k} \tag{13}$$

where k is the order chosen for the system identification method.

Due to nonlinearities, non-proportional damping, and possible noise, the obtained modes by the system identification can be complex. In Rainieri and Fabbrocino [15] a discussion of those complex modes from system identification and an approach, used in the present work, to convert them to real mode shapes is presented. The mode shapes can be obtained by adding the real modes of displacements with the initial equilibrium condition.

As the method is meant to a linear system, the choice of inputs (in this case, loads) should be such that the system behaves approximately linear. Also, for better accuracy, the number of frequencies determined should be no more than the number of POD modes selected.

4 Numerical Studies

4.1 Simulation Details

A verification of the POD combined with system identification (sys ID) is first performed by a purely structural case and then the method is applied for the stability analysis of the aeroelastic cases. For these studies, two models are used: i) the University of Michigan's X-HALE UAS [16] for the purely structural case and ii) the University of Michigan's X-HALE UAS with an added tip mass of 0.5 kg located 0.36 m behind the wing trailing edge for the aeroelastic cases. This tip mass was added such that the model could present unstable aeroelastic behavior in a range of velocities within the aircraft flight envelope. As shown in Figure 1, the X-

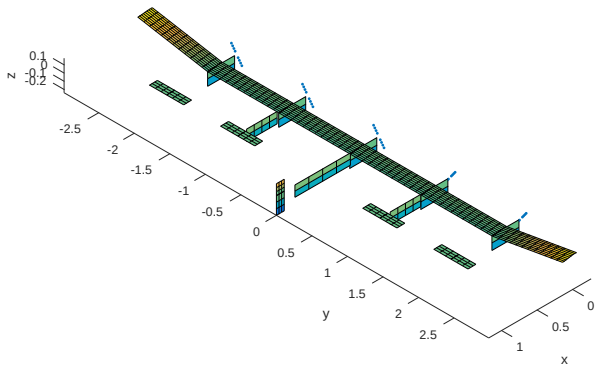

Fig. 1 : Undeformed panel model for the X-HALE UAS vehicle (units: meters)

HALE has a wingspan of 6 m with a 0.2-m chord, five pods along the wing, five tails, three fins and five electric motor-propeller combinations located in front of each pod at spanwise locations $y = -2, -1, 0, 1$, and 2 meters. The wing is mounted with an incidence angle of 5 degrees. For the simulations, the propellers are located 20 cm ahead and 2.8 cm below of the wing leading edge, with a pitch angle of 5 degrees between the propeller axis and the X-HALE wing, as the wing has an incidence angle with respect to the pods. In order to reduce asymmetric loads, the propellers on the right wing have a different direction of rotation with relation to propellers at the left wing. A summary of the propeller parameters used here is presented in Table 1 and more details can be found in [13]. A cut-off distance of two radius after the end of the X-HALE vertical tails was applied to save computational cost. In the aeroelastic solver a stiffness-proportional damping coefficient of 0.005 s and a time step of 0.002 s (for 6000 RPM) and 0.0017 (for 7000 RPM) were considered (with a sub-time step of half structural step). The dynamic viscosity is $\mu = 1.7855\ 10^5$ N.s/m^2 and the air density $\rho_\infty = 1.225$ kg/m^3. For the aeroelastic cases, gravity effects are also considered.

Table 1: Two-bladed APC 11X5.5E propeller parameters

Blade properties	APC 11X5.5 E
Airfoil type	NACA 4412
Propeller mass	0.023 kg
Number of blades	2
Blade discretization	4 segments
Time step	$T_P/10$
Sigma particles	0.0195

4.2 Verifying POD + Sys ID for Purely Structural Case

In order to verify the capability of the POD + sys ID to extract frequency, damping, and modes of the flexible model, a purely structural case was used for which a reference from UM/NAST modal solver was available about its undeformed shape. For the POD + Sys ID, a time simulation was performed for the clamped model from the undeformed configuration disturbed after 1.5 s by a 5 Nm torsion moment and a 1 N step force in the vertical and chordwise direction, all applied at the right wing tip of the clamped model and chosen to excite different modes. The snapshots were then provided to the POD + Sys ID method, 5 POD modes were used (contributing for more than 99% of the snapshot energy) and an order of 18 was chosen for the system identification method based on the fitting quality of the POD coefficients. As the reference was for the undeformed, undamped case, no gravity or damping effects was included. Also, as the identification order of 18 provides 9 frequencies, but just 5 POD modes are used (and up to 5 frequencies can be more accurately identified), the main frequencies were determined by choosing the five higher norms of the corresponding coefficients identified for the POD modes. Therefore the frequencies associated to the five columns of $C_{p\times k}E_{k\times k}$ with higher Euclidean norms were kept and shown in Figure 2.

Table 2 presents the comparison between frequencies as well as a comparison of the corresponding modes by applying Model Assurance Criteria (MAC). For this purely structural case, one can see the method had an excellent agreement with the data calculated by the modal solver in UM/NAST with a maximum error in frequency prediction smaller than 2% and a MAC value of about 0.99 for all five modes.

Table 2: Comparison of natural frequencies for purely structural case

UM/NAST	POD + SysID	Error (%)	MAC
0.5943 Hz	0.5923 Hz	−0.3422	0.9879
2.5747 Hz	2.5299 Hz	−1.7407	0.9896
3.6986 Hz	3.6631 Hz	−0.9596	0.9922
4.4491 Hz	4.4900 Hz	0.9195	0.9937
6.5696 Hz	6.5286 Hz	−0.6241	0.9980

(a) First bending (UM/NAST): 0.5943 Hz

(b) First bending (POD + SysID): 0.5923 Hz

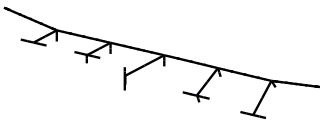

(c) First torsion (UM/NAST): 2.5747 Hz

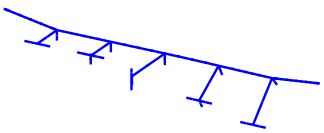

(d) First torsion (POD + SysID): 2.5299 Hz

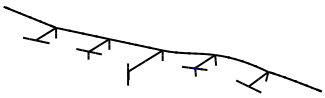

(e) Second bending (UM/NAST): 3.6986 Hz

(f) Second bending (POD + SysID): 3.6631 Hz

(g) First in-plane bending (UM/NAST): 4.4491 hZ

(h) First in-plane bending (POD + SysID): 4.4900 Hz

(i) Second torsion (UM/NAST): 6.5696 Hz

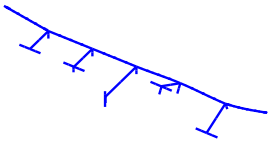

(j) Second torsion (POD + SysID): 6.5286 Hz

Fig. 2 : Comparison of mode shapes and natural frequencies for the X-HALE UAS vehicle about its undeformed configuration

4.3 Influence of the inclusion of Aerodynamic and Gyroscopic Propeller Effects on the Aeroelastic Stability

In order to check the additional influence of propeller slipstream and gyroscopic effects, besides the influence of thrust (already investigated by, e. g., Hodges *et al.* [4]), transient solutions for a clamped aeroelastic case were conducted. Beginning from an equilibrium state and after 1.5 seconds of simulation, a step perturbation of 5 Nm in torsion moment and a 1 N step force in vertical and chordwise directions were applied. In this case, gravity and a stiffness-proportional damping coefficient of 0.005 s were considered, to have a more realistic response. Three cases with velocities: 12.5 m/s, 13 m/s and 13.5 m/s were simulated for a model with just thrust at the propeller location (equivalent to the thrust produced by the isolated propeller at each velocity for the considered RPM) and a complete propeller model, including thrust (and other loads at hub), slipstream, and gyroscopic effects, with a rotation of 6000 RPM.

First, the same set of parameters determined in the verification case was tried (5 POD modes and Sys ID order of 18), but for the cases with aerodynamic and, for some of them, gyroscopic moment, the adjusting of the 5th POD coefficient using the same set of parameters for all cases was hard to get (especially for cases after the flutter boundary). Then, just 4 POD modes were consid-

ered (representing more than 99% of the snapshot energy), and an order of 18 was again included, improving the fitting of the first 4 POD coefficients. For the purely structural case the effect of reducing the POD modes to 4, keeping the same order for the Sys ID, was of reducing the accuracy of higher frequencies, but the 4 first frequencies were kept with good precision (smaller than 2% error). Then, for the cases in this section, just 4 frequencies and modes are compared, which correspond to the most important modes for the system response. Also, the sensitivity of the results with the number of snapshots provided before the perturbation starts was found to be higher for cases with higher numerical perturbations, as in the cases after flutter. All cases use the same set of parameters and it is expected that the results can capture frequency variations due to the different effects being modeled.

Figure 3 presents a comparison of the frequencies, dampings, and dynamic responses in terms of wing tip vertical and angular displacements for each velocity simulated. From the dynamic responses, it is possible to see that for this model and propeller RPM the flutter boundary is about 13 m/s for both cases, i. e., thrust only, and including complete propeller modeling. However, as one can also observe by the dynamic responses, for all speeds increasing differences in phase arise between cases with thrust only and with all propeller effects. For the same set of POD + Sys ID parameter choice, one can also note differences of frequencies and especially damping for modes more distant from the stability boundary. Considering that the variations of frequency and damping are captured, this indicates propellers can affect dynamic response.

4.4 Influence of Increasing Propeller RPM

In order to investigate the effect of propeller RPM in the aeroelastic stability, a transient solution similar to the one presented in Figure 3 was simulated at $v = 13$ m/s, however with a higher propeller rotation, 7000 RPM. Increasing the propeller RPM with all other parameters constant means a higher influence on the velocity flowfield behind the propeller's plane of rotation, as well as a higher thrust and gyroscopic loads. It can be interpreted as the degree of propeller effects intensity, which could be affected also by other parameters like propeller mass, geometry, velocity flowfield, etc.

Figure 4 presents a comparison of the wing tip dynamic responses. Now, more noticeable differences can be observed in the stability behavior: while the case with 6000 RPM is yet stable (although close to flutter), the case with 7000 RPM shows an unstable behavior with increasing amplitudes, then a lower flutter speed. This example indicates that depending on the intensity of propeller effects the influence on stability boundary can be more significant. Damping and frequency were not compared, as the same set of parameters used in $v = 13$ m/s for 6000 RPM does not provide a good fitting for the case of 7000 RPM.

4.5 Contribution of Different Propeller Effect Components

Figure 5 compares the dynamic response as well as frequency and damping for the same disturbance as in Figure 4 at $v = 13$ m/s. This case is already in the unstable regime. Due to more difficulties in find a common set of parameters with good fitting and in order to reduce the perturbation due to numerical noise, just three POD modes were incorporated (representing more than 97% of the snapshot energy), keeping the identification order as 18, and the snapshots were provided with 0.5 second after beginning of perturbations.

In order to observe the isolated propeller effect components (mainly thrust, slipstream and gyroscopic moment) three different modeling of propeller effects are considered: i) with thrust only (equivalent to thrust produced by isolated propeller at $v = 13$ m/s and 7000 RPM), ii) with thrust (and other loads at hub) and slipstream (propeller aero), and iii) with thrust (and other loads at hub), slipstream and gyroscopic effects (propeller aero + gyro). From the dynamic response, it is clear that the inclusion of propeller

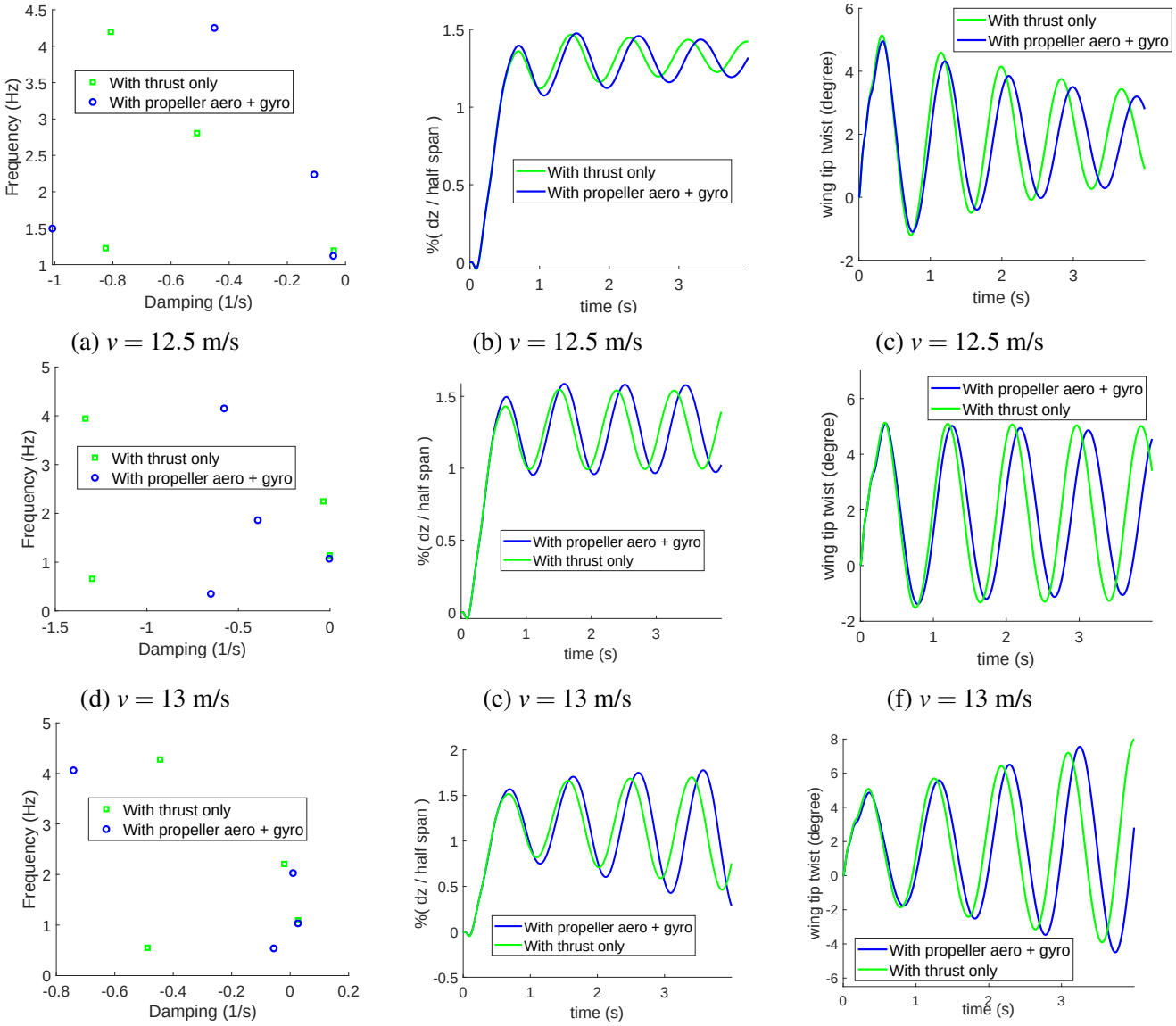

(a) $v = 12.5$ m/s (b) $v = 12.5$ m/s (c) $v = 12.5$ m/s

(d) $v = 13$ m/s (e) $v = 13$ m/s (f) $v = 13$ m/s

(g) $v = 13.5$ m/s (h) $v = 13.5$ m/s (i) $v = 13.5$ m/s

Fig. 3 : Frequencies, dampings, and response after perturbation with step loads of 5 N in vertical and chordwise direction and 1 Nm in torsion (6000 RPM)

aerodynamic effects can cause a non-negligible difference in the aeroelastic stability, with the model including just thrust having a smoother amplitude increase, suggesting a higher flutter boundary. An increasing difference of phase with time is also noticeable between the case with just thrust and other two cases. The inclusion of gyroscopic effects causes negligible differences for vertical displacements but more visible differences in the amplitude of angular displacement, which is smaller for the case including gyroscopic effects. This is in accordance with the root locus, where it is clear that the positive damping for the unstable modes in the case with slipstream and no gyroscopic effects is higher, suggesting the gyroscopic effect has a stabilizing effect.

4.6 Concluding Remarks

This work investigated the influence of propeller aerodynamics, and gyroscopic effects on the aeroelastic stability of very flexible aircraft. For that, an enhanced aeroelastic framework with

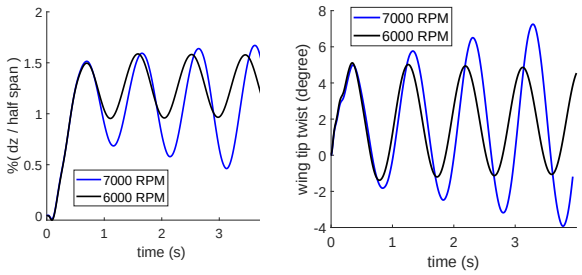

(a) Tip vertical displacement

(b) Tip twist

Fig. 4 : Wing tip response after perturbation with step loads of 5N in vertical and chordwise direction and 1Nm in torsion, including propeller aerodynamics and gyroscopic effects

propellers developed in previous efforts by the authors [17], [13] was applied to extract time-data snapshots of the clamped modified X-HALE UAS representing a HALE aircraft. A method based on POD plus system identification to extract frequencies, dampings, and modes from the time-series data was successfully verified for a purely structural case for which a reference solution was available. The method was then used to analyze the effect of the propeller on the aeroelastic stability of the very flexible aircraft based on a set of generated snapshots. From the analysis of aeroelastic cases and the clamped model considered, it was observed that the presence of propeller aerodynamic and gyroscopic effects influences the values of damping and frequencies of some modes and can influence stability boundary. Moreover, an increase in phase delay and differences in amplitude in the response to a perturbation close to flutter were shown as compared to the case with just thrust. A reduction of flutter boundary was found by an increase in propeller RPM. Also, a slight stabilizing effect due to the gyroscopic moment was noticed, suggesting this effect may be more important for cases with higher gyroscopic moment loads, i. e., higher RPM and propeller mass. Finally, the method of POD plus system identification showed to be effective to extract frequencies, dampings, and modes for a purely structural case. Further investigations are necessary to make the method more robust for aeroelastic cases.

References

[1] Phillips W. *Mechanics of flight*. Wiley, 2004.

[2] Ribner H S. Propellers in yaw. National advisory committee for aeronautics, 1945.

[3] Bouquet T. *Modelling the propeller slipstream effect on the longitudinal stability and control*. Master's thesis, Delft University of Technology, 2016.

[4] Hodges D H, Patil M J and Chae S. Effect of thrust on bending-torsion flutter of wings. *Journal of Aircraft*, Vol. 39, No. 2, pp. 371–376, 2002.

[5] Feldt W T and Herrmann G. Bending-torsional flutter of a cantilevered wing containing a tip mass and subject to a transverse follower force. *Journal of the Franklin Institute*, pp. 467–468, 1974.

[6] Quanlong C, Jinglong H and Haiwei. Effect of thrust engine on nonlinear flutter of wings. *Journal of Vibroengineering*, pp. 1731–1739, 2013.

[7] Shearer C M and Cesnik C E S. Nonlinear flight dynamics of very flexible aircraft. *Journal of Aircraft*, Vol. 44, No. 5, pp. 1528–1545, 2007.

[8] Su W and Cesnik C E S. Strain-based geometrically nonlinear beam formulation for modeling very flexible aircraft. *International Journal of Solids and Structures*, Vol. 48, No. 16-17, pp. 2349âĂŞ–2360, 2011.

[9] Ritter M, Cesnik C E S and Kruger W R. An enhanced modal approach for large deformation modeling of wing-like structures. In *AIAA Science and Technology Forum and Exposition*. 2015. Kissimmee, Florida, 5-9 January 2015. AIAA 2015-0176, 10.2514/6.2015-0176.

[10] Singh P and Friedmann P P. Application of vortex methods to coaxial rotor wake and load calculations in hover. *Journal of Aircraft*, 2017.

[11] He C and Zhao J. Modeling rotor wake dynamics with viscous vortex particle method. *AIAA Journal*, Vol. 47, No. 4, pp. 902–915, 2009.

[12] Winckelmans G S and Leonard A. Contributions to vortex particle methods for the computation of three-dimensional incompressible unsteady flows. *Journal of Computational Physics*, Vol. 109, No. 2, pp. 247–273, 1993.

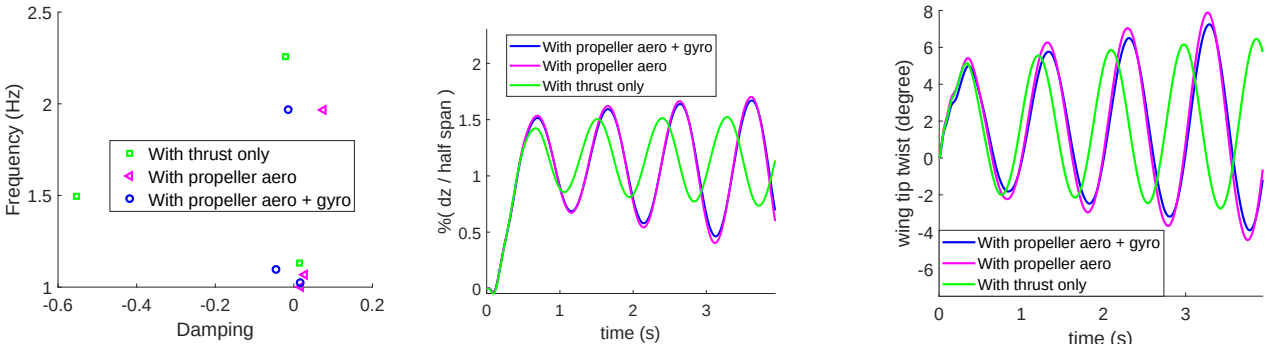

(a) Root locus (b) Wing tip vertical displacement (c) Wing tip twist

Fig. 5 : Frequencies, dampings, and response after perturbation with step loads of 5 N in vertical and chordwise direction and 1 Nm in torsion (7000 RPM)

[13] Teixeira P C and Cesnik C E S. Propeller effects on the dynamic response of hale aircraft. In *AIAA/ASCE/AHS/ASC Structures, Structural Dynamics, and Materials Conference, AIAA SciTech Forum*. 2018. Kissimmee, Florida, 8âĂŞ12 January.

[14] Van Overschee P and De Moor B. N4sid: Subspace algorithms for the identification of combined deterministic-stochastic systems. Automatica, Vol. 11, No. 2, 1963, pp. 431-441. doi: 10.1137/0111030.

[15] Rainiere C and Fabbrocino G. *Operational modal analysis of civil engineering structures*. Spring-Verlag New York, 2014.

[16] Cesnik C E S, Senatore P J, Su W, Atkins E M and Shearer C M. X-hale: A very flexible unmanned aerial vehicle for nonlinear aeroelastic tests. *AIAA Journal*, Vol. 50, No. 12, pp. 2820–2833, 2012.

[17] Teixeira P C and Cesnik C E S. Inclusion of propeller effects on aeroelastic behavior of very flexible aircraft. In *International Forum on Aeroelasticity and Structural Dynamics, IFASD 2017*. Como, Italy, 25-28 June 2017.

5 Contact Author Email Address

Patricia Teixeira: pct@umich.edu

Copyright Statement